

**Symmetry-reversals in chiral active matter**

Journal:	<i>Soft Matter</i>
Manuscript ID	SM-ART-02-2018-000402.R1
Article Type:	Paper
Date Submitted by the Author:	22-May-2018
Complete List of Authors:	Workamp, Marcel; Wageningen University & Research, Physical Chemistry and Soft Matter Ramirez, Gustavo; Hunter College; North Carolina State University, Department of Physics Daniels, Karen; North Carolina State University, Department of Physics Dijksman, Joshua; Wageningen University, Physical Chemistry and Colloid Science



Cite this: DOI: 10.1039/xxxxxxxxxx

Symmetry-reversals in chiral active matter[†]

Marcel Workamp,^a Gustavo Ramirez,^{b,c} Karen E. Daniels^c and Joshua A. Dijksman^a

Received Date

Accepted Date

DOI: 10.1039/xxxxxxxxxx

www.rsc.org/journalname

We perform experiments on an active granular material composed of individually-driven, spinning disks confined within a circular arena. Small bumps at the outer edges of the disks provide a variable amount of interparticle coupling in the form of geometric friction. The disks each spin counter-clockwise, but undergo a transition in their collective circulation around the center of the arena, from a clockwise orbit to a counter-clockwise orbit, as a function of packing fraction ϕ . We identify that, unlike for vibrated granular gases, the particles' velocity distributions are Gaussian over a large range of ϕ . By fitting the speed distribution to a Maxwell-Boltzmann distribution, we identify a temperature-like parameter which is a universal function of ϕ ; this parameter is also equal to the mean translational energy of the particles. We quantify the collective circulation via its solid-body-like rotation rate, and find that this is a universal function centered around a critical packing fraction. In addition, the ratio of orbital kinetic energy to spin kinetic energy is also a universal function for non-zero geometric friction. These findings highlight the important role of both the type of driving and the interparticle interactions (here, geometric friction) in controlling the collective behavior of active granular systems.

1 Introduction

In nature, individually-driven particles commonly display complex collective phenomena, ranging from tiny microtubule assemblies to giant schools of fish and bird flocks. Both the driving mechanism and the inter-particle interactions are known to play important roles in determining how correlated motions arise in active matter^{1–8}, but it remains an open question how to exploit these control parameters to develop new materials and devices with functionalities absent in passive matter^{9–11}.

Motivated by biological systems, studies of the origins of collective motion have often been on self-propelled particles rather than self-spinning particles. A key difference is that spinning particles are fundamentally chiral rather than anisotropic, and therefore present an interesting contrast. Simulations of active-spinner particles display interesting collective phenomena such as reversal of the forces between active particles in a passive medium¹², as well as complex phase behavior^{13–15}. In experiments with colloids, spinners driven by magnetic fields can generate chaotic fluid flow reminiscent of turbulence¹⁶, while electric fields can be used to assemble Janus particles into rotating pinwheels which may syn-

chronize their rotation direction¹⁷.

Active spinning may also be achieved in vibrated granular materials^{18–22}, through the use of asymmetric particles driven by the shaking of a quasi-two-dimensional container. These studies have demonstrated that spinning particles display some key thermal-like properties, since the translational degrees of freedom are no longer actively- or boundary-driven: the particles only acquire translational momentum through either collisions or hydrodynamic interactions.

It is important to contrast active systems with ordinary granular gases,^{23,24} in which energy is strongly injected at the boundary/system scale rather than at the particle scale. Granular gases may display collective phenomena, such as clustering^{24–26} and giant number fluctuations²⁷. While all granular gases are strongly non-equilibrium due to combined effects of driving and dissipation, they nonetheless display many features of molecular gases, such as Brownian motion²⁸ and equipartition of kinetic energy among the available degrees of freedom²⁹. However, in contrast to molecular gases, the velocity distribution in granular gases is typically not a Gaussian. Instead, high energy tails are usually observed, with distributions that instead fall off either exponentially or as $P(v) \sim \exp(-v^{\frac{3}{2}})$ (see Ref.^{30–33}), in agreement with kinetic theory of granular gases³⁴. Because the particles in a typical granular gas obtain their momentum from the boundaries, one may expect the structure of these boundaries to influence the distribution. Indeed, when rough boundaries are used, the transfer and randomization of linear momentum is more effective than for smooth boundaries, and the velocity distributions may approach

^a Physical Chemistry and Soft Matter, Wageningen University & Research, Wageningen, The Netherlands

^b Hunter College, City University of New York, New York, NY, USA.

^c Department of Physics, North Carolina State University, Raleigh, NC, USA.

[†] Electronic Supplementary Information (ESI) available: 3D-drawings of the particles (STL format), video of particles with $l = 2$ mm at varying packing fractions. See DOI: 10.1039/cXsm00000x/

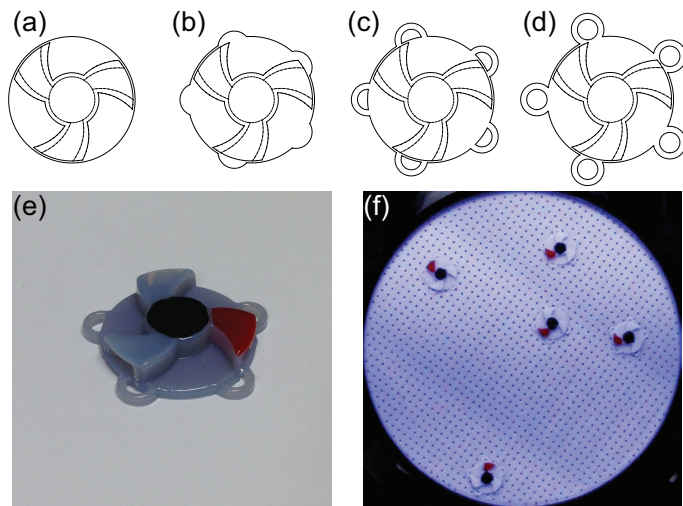


Fig. 1 (a-d) Top view of the particles, which spin in a counter-clockwise (CCW) direction due to air pushed outward through each of three channels. The main disk diameter is 15.5 mm, the diameter of the hole in the bottom is 5.6 mm, and the diameter of the disks that make up the bumps is 4 mm. From (a) to (d), the amount the bumps protrude from the main circle is $l = 0, 1, 2,$ and 3.25 mm respectively. (e) Photo of a 3D-printed particle with $l = 2$ mm. Black and red labels are used to facilitate tracking of particle position and orientation. (f) Video still from an experimental video, showing the hole pattern in the air table surface.

a Gaussian³⁵.

In this paper, we experimentally investigate the mechanics of an active granular material, from the gas phase through to an orbiting-solid phase, and finally a transition to dynamic arrest due to crowding. In contrast to the granular gases with asymmetric particles described in References^{18,20,21}, our particles are driven at the particle scale: each particle experiences a continuous, finite torque by drawing energy from an air flow. However, the interparticle interactions remain typical of granular materials, with frictional contacts and inelastic collisions. Inspired by numerical simulations from Nguyen *et al.*¹³, we 3D-print disks with protruding peripheral bumps to provide the particles with a tunable geometric friction (see Fig. 1). These chiral airfoil particles are levitated on an air table to eliminate friction with the base. Each particle has a hole in the center of its base, through which air from the table enters. This air exits the particles through three channels aimed to provide the particle with a finite, constant torque. Thus, like the particles presented in the accompanying paper by Farhadi *et al.*³⁶, they draw their activity from the same air flow that levitates them.

Our experiments are performed on systems containing a variable number of counter-clockwise (CCW) spinning particles contained within a fixed circular arena. At low packing fraction ϕ , at which the particles are largely non-interacting, the average translational motion of the particles is in the clockwise (CW) direction with respect to the center of the arena. Above a critical packing fraction ϕ_c , a collective mode develops in which solid-body orbital motion occurs in a CCW direction. This symmetry-reversal arises through interparticle-interactions coupling the particles' rotational and translational degrees of freedom, and the value of ϕ_c is therefore found to be dependent on the bump size l .

These findings are supplemented by an examination of the underlying thermal-like nature of the system. For fixed l and varying packing fraction ϕ , we find that the velocity distributions of the individual particles is approximately Gaussian over a large range of ϕ , and can be well-described by a Maxwell-Boltzmann distribution of speeds. We find that the thermal energy measured by fitting these distributions is a universal function of ϕ for non-zero l , and is equal to the translational kinetic energy of the particles. While this suggests that the tools of statistical physics would work over a large range of ϕ , there is an important caveat. We also find that the partition of energy between orbital and spin modes is dependent on both ϕ and the presence of geometric friction. Together, these findings demonstrate the importance of the specific type of driving to the mechanics of driven granular/active systems, and highlights the role of geometric friction in the emergence of collective behavior.

2 Materials & Methods

2.1 Particle design

The experimental system is based on flat-bottomed disks (airfoils) floating on an air table. The particles are 3D-printed pinwheels, designed to draw air in through a central hole and out through three channels, as shown in Fig. 1. Because the channels are directed at an angle relative to the radial direction, the exiting air provides a torque on the particle, causing it to spin. In order to maximize the torque and generate fast spinners, we conducted tests systematically varying a single particle's design parameters. We found that an optimum shape for a particle with low mass (low moment of inertia) was made possible by having a low number of wide channels, and an intake hole of comparable size to the channel width. All particle design was done using SolidWorks software; high resolution STL files of the particles are available in the Electronic Supplementary Information (ESI).

In the final design, the particles were printed on a Stratasys Object 30 Scholar 3D-printer, with a main disk of diameter 15.5 mm, and a central hole of diameter 5.6 mm. We vary the magnitude of the interparticle interactions by adding five circular bumps to the periphery, each of diameter 4 mm but with a variable amount of protrusion ($l = 0, 1, 2$ or 3.25 mm) shown in Fig. 1a-d. This results in a tunable amount of *geometric friction* between the particles³⁷.

2.2 Air table setup

The particles levitate on an air table, which both eliminates basal friction and supplies the required energy to spin the particles. The table is designed to mimic commercial air-hockey tables, with the top surface perforated with holes approximately 1 mm in diameter, in a square pattern with separation 3.5 mm between holes (see Fig. 1f); like the particles, this surface is also 3D printed. The circular arena in which the particles are confined has a diameter of 150 mm.

Air is supplied to the air table surface as follows. Two building-supplied compressed air lines (0.6 MPa each) are connected to a single manifold with four outlets using 8 mm pneumatic tubing. The four outlets are connected to a 3D-printed plate sealed to a

125 mm tube. Directly behind the plate, on the inside of the tube, a stainless steel wire sponge homogenizes the air flow. A subsequent adapter widens the tube from 125 to 150 mm. The air table surface is placed on top of the tube and the connection is sealed using Parafilm. Additional details are available elsewhere³⁸.

Leveling of the table is crucial, because the particles would otherwise experience a gravitational field. After initial leveling with a high resolution bubble level, we check that the table is level by recording a video with approximately 10 particles from which we obtain the particle positions (see §2.3), and compute a 2D histogram of these positions. We level the table via its adjustable feet until this 2D histogram is symmetric around the center of the arena.

2.3 Imaging and particle tracking

We track particle positions and orientations from above using a Canon EOS 70D DSLR camera in video mode, at a frame rate of 50 Hz. We illuminate the experiment using a high powered LED lamp. Since the finish of the 3D-printed materials is glossy, we place polarizers in front of the lamp as well as the camera lens, to block reflections from the particles or air table. In each experiment, we image the particles for a total of 10^4 frames, corresponding to 200 seconds. To obtain contrast with the table surface, we mark the center of each particle with a black marker, and one of the 3 air channels with a red marker (see Fig. 1ef). We locate the particles by finding the center of mass of each black dot, and measure each particle's orientation using the four-quadrant inverse tangent of the relative position of the black and red marks.

In contrast to typical particle tracking applications (e.g. microscopy on colloidal systems), we have selected number of particles N in each dataset. Therefore, our particle-locating scripts are designed to locate exactly N particles in each frame. To find the trajectories of the particles we use tracking algorithms initially developed by D. Grier, J. Crocker and E. Weeks, adapted to MATLAB and made available online by D. Blair and E. Dufresne³⁹. When the maximum distance traveled per frame is set to a sufficiently small number, we successfully obtain exactly N trajectories. The orientation of each particle is specified in the range $-\pi < \theta \leq \pi$, and therefore a time-series $\theta(t)$ for a freely-spinning particle is discontinuous at each $\pm 2\pi$ jump. We resolve this issue by adding (or subtracting) 2π when the sign of the orientation angle changes from positive to negative (or negative to positive) values, so that $\theta(t)$ is a continuous function.

2.4 Particle characterization

We characterize the particles by determining their weight, moment of inertia, and driving torque. Since the torque depends on the air flow of the air table and thus on the air pressure from the building's outlets, we perform all experiments in quick succession to avoid a possible dependence on fluctuations in pressure. We measure the torque T of the particles by measuring the angular acceleration $\ddot{\theta}$ of a particle after a collision. As shown in Fig 2, plots of $\theta(t)$ are initially quadratic, and we fit the data with a purely quadratic function to obtain $\ddot{\theta}$. We calculate the torque from $T = I\ddot{\theta}$, with I the moment of inertia about the z -axis (the

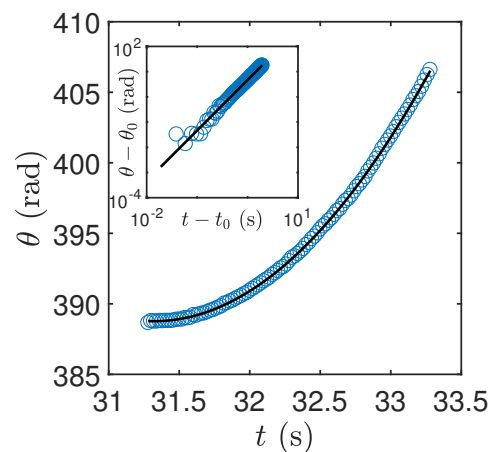


Fig. 2 Time-series of the orientation $\theta(t)$ of a $l = 2$ mm particle after a collision with the wall. The solid line represents a quadratic fit, from which we obtain the torque. Inset shows the same data relative to its initial orientation at $\theta_0 = \theta(t_0)$, plotted on logarithmic axes to illustrate the purely quadratic nature of $\theta(t)$.

symmetry axis of the particle). Ultimately, an isolated particle reaches a terminal spin rate due to drag.

Rather than measure I directly, we instead use the value provided by the SolidWorks design software. Due to small imperfections in the 3D-printing process, we find that the real mass m differs from the predicted value m_s , by approximately 10%. To correct I for this difference, we multiply the SolidWorks-provided value by the ratio of m/m_s . The particles have masses m ranging from 0.34 to 0.40 g, while their corrected moment of inertia ranges 10.4 to 14.4 g·mm². We find the torque T of the particles to be approximately 5.5×10^{-8} Nm.

3 Results & discussion

3.1 Phenomenology

We perform experiments by varying the number of particles N placed within an arena of fixed area A_a . This is conveniently characterized the packing fraction $\phi = NA_p/A_a$, where A_p is the cross-sectional area of single particle (including the bumps). We increase N in steps of single particles from $N = 2$ up to $N = 5$, and steps of two or more particles from $N = 5$ until the collection of particles start to slow down again due to crowding. Movies of these dynamics are available in the ESI. In this work, we focus on symmetry reversal at low to intermediate ϕ ; we leave the slow-down of dynamics at high ϕ for future work. At a critical ϕ (which likely depends on the bump size), these systems will eventually jam completely.

From the particle positions and orientations, we calculate both their translational velocity \vec{v} and their spinning rate $\omega \equiv \dot{\theta}$. We measure (\vec{v}, ω) from the difference in particle (positions, orientations) between consecutive frames. We have verified that our main results do not depend significantly on the time step chosen; changing the time step from 1 to 8 frames yields similar results.

At very low packing fraction ϕ , we observe that although the particles' own spin direction is counter-clockwise (CCW), their average orbital motion is instead in a clockwise (CW) direction with respect to the center of the arena, as illustrated in Fig. 3a.

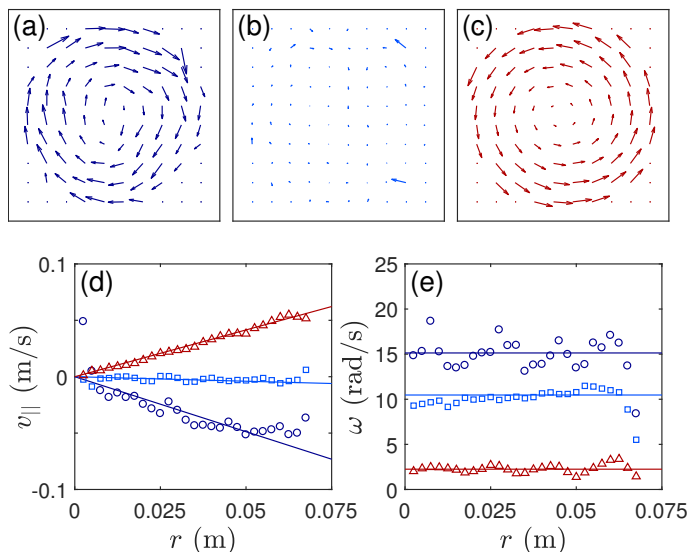


Fig. 3 Representative data showing the onset of collective behavior, for CCW-spinning particles with $l = 2$ mm. (a-c) Vector fields showing the average translational velocity \bar{v} for (a) $N = 2$ ($\phi = 0.025$), (b) $N = 7$ ($\phi_c = 0.088$), and (c) $N = 45$ ($\phi = 0.564$) particles in the circular arena. All vectors in (a,b,c) are drawn using the same scale on the same grid, and represent the Eulerian velocity field (not the velocity of individual particles). The orbit reverses from CW at low ϕ to CCW at high ϕ , and (b) is selected to be at ϕ_c . (d) Average orbital velocity $v_{||}$ for individual particles, binned by their radial position r , for $N = 2$ (\circ), $N = 7$ (\square), and $N = 45$ (\triangle) particles. Solid lines represent $v_{||} = \bar{\Omega}r$ calculated for the ensemble. (e) Average particle spin rate ω for individual particles, binned by their radial position r and using the same symbols as in (d). Movies of these dynamics are available in the ESI.

In contrast, for high ϕ , the average orbital motion becomes CCW, as shown in panel (c). Between these two cases, we observe a critical value ϕ_c at which the orbital motion of the particles is on average zero, shown in panel (b). Due to the circular geometry, it is helpful to consider the orbital (azimuthal) velocity component of these vector fields, denoted by $v_{||}$. As can be seen in panel (d), $v_{||}$ switches from negative (CW) to positive (CCW) as a function of ϕ . For other values of bump size l , the value of ϕ_c shifts, but the same phenomenology occurs. Thus, we also find collective behavior in systems of bump-less disks, in contrast to the findings presented by Farhadi *et al.*³⁶ A possible explanation for this difference is that translation appears to play a bigger role in our system; we find that in dilute systems the ratio of rotational and translational energy is of order 10 (see Section 3.3), whereas Farhadi *et al.* report values of order 10^3 . We observe that particles occasionally get a random "kick" from the air flow field, an effect that can easily be observed at low ϕ (Movies of these dynamics are available in the ESI). This increased translation leads to more collisions in which the rotational and translational degrees of freedom are coupled through friction.

We define the average orbital rotation rate of our collective material as

$$\bar{\Omega} = \left\langle \frac{1}{N} \sum \frac{v_{||,i}}{r_i} \right\rangle_t \quad (1)$$

where the summation is over N particles labeled with the index i , $v_{||,i}$ is the orbital velocity component of the i -th particle, and

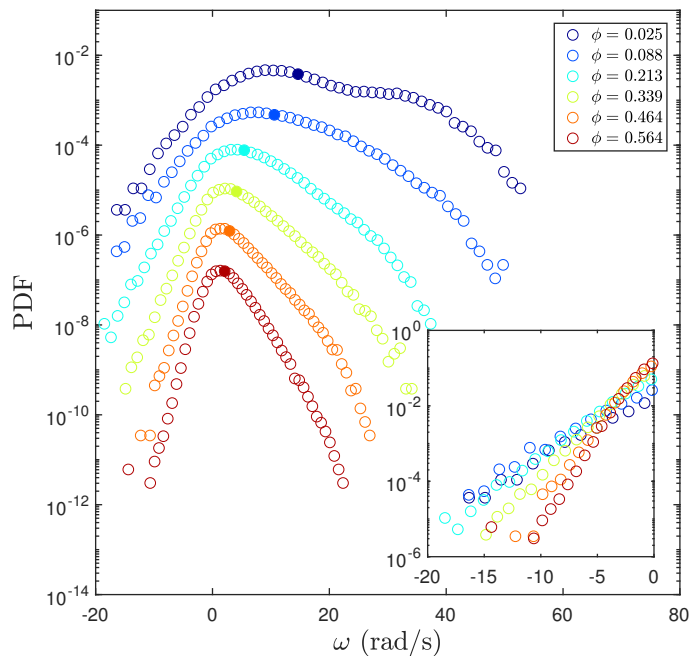


Fig. 4 Probability density function (PDF) of the spin rate ω for particles with $l = 2$ mm, for six representative values of ϕ . Filled symbols represent the mean $\bar{\omega}$. For better visibility, the curves are shifted vertically. Inset shows the PDF of negative ω without vertical shift. The probability of negative ω decreases with ϕ .

r_i is its radial position. The final average is over all times. Each solid line in Fig. 3d represents $v_{||} = \bar{\Omega}r$, with $\bar{\Omega}$ determining the slope of the line. The linearity of the local $v_{||}$ (symbols), particularly at high ϕ , indicates that a symmetry-reversal transition induces a state of (on average) solid-body rotation. Solid-body rotation has been observed previously in self-propelled particle systems^{40,41}, where particles were shown to organize in a rotating lattice. However, in our experiments, the particles do not form a rotating lattice (their relative positions are not fixed), and have enough freedom to spin individually.

As shown in Fig. 3e, the average spin rate ω of individual particles is independent of their position within the arena, but strongly dependent on ϕ . We observe that ω decreases with ϕ , which we interpret as arising because the time between collisions decreases at larger ϕ . This provides less time for the particles to accelerate to high ω between collisions.

There are a few caveats about data-collection at low ϕ . In this regime, we occasionally observe ω values large enough that they are difficult to quantify given the frame rate of the camera. Because these instances are rare, they only marginally affect quantities such as the mean rotational kinetic energy of the particles. For bump-less particles ($l = 0$ mm) at $\phi < 0.16$, there is an instability in which all particles quickly find a steady state in which they simply orbit at the boundary of the arena. In this state, $v_{||} = \text{const.}$ and they have no interactions or collisions with each other. We have therefore excluded these datasets from our analysis.

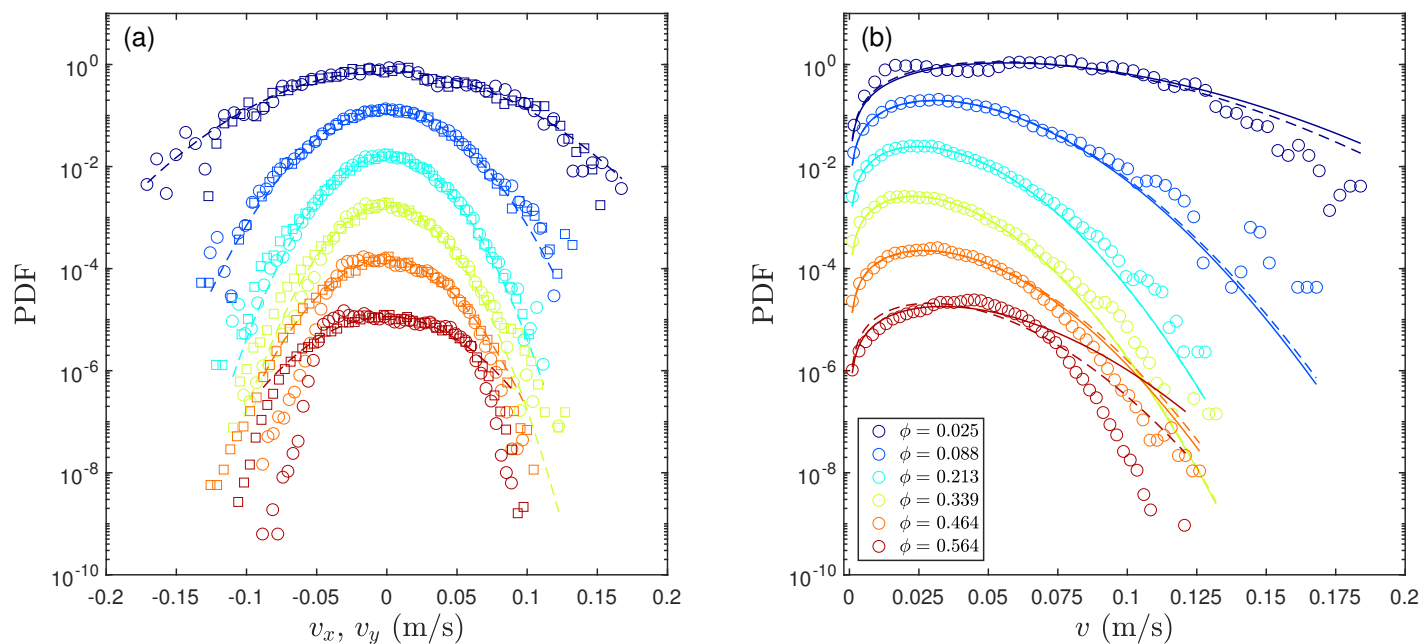


Fig. 5 (a) Probability density function (PDF) of the speeds v_x (\circ) and v_y (\square) for particles with $l = 2$ mm, for six different packing fractions. Dashed lines represent Gaussian fits. For better visibility, the curves are shifted vertically. (b) Probability density function (PDF) of the speed v for particles with $l = 2$ mm, for six different packing fractions. Solid lines represent a fit using Eq. 2, dashed lines represent predictions obtained by extracting kT_{eff} from the Gaussian fits of the PDF of v_x , see panel (a). For better visibility, the curves are shifted vertically. Legend in (b) applies to both panels.

3.2 Speed distributions

We first consider the distribution of measured values of the spin rate ω . The spin direction is, on average, in the CCW direction due to the chirality of the particle-design, but through collisions particles can spin in either direction. As shown in Fig. 4, this leads the probability density function (PDF) $P(\omega)$ to be asymmetric. We observe that the mean spin rate $\bar{\omega}$, shown by the filled symbols, depends strongly on ϕ and remains positive due to the continual torque provided by the air channels. There is a trend in the shapes of these distributions from broad and high-valued at low ϕ to narrow and small-valued at high ϕ . This arises because, at lower ϕ , there is a longer time between collisions, leaving time for the particles to accelerate to high ω and less chance of a collision causing a reversal of spin direction.

Importantly, negative ω values are observed at all ϕ , with the probability decaying roughly exponentially away from the peak of the distribution (see inset Fig. 4). The ϕ -dependence of this probability can be qualitatively explained by considering two particles (i, j) engaged a head-on collision. If the two particles are spinning in the same direction, at the point of contact the edges/bumps are moving in opposite directions. For $\omega_i > \omega_j$, particle j receives an impulse that reverses its spin direction. Since at low ϕ , much higher ω can be achieved, the difference between the spinning rates of the two colliding particles may be larger, leading to increased probability of large negative ω (see inset Fig. 4). Note that at low ϕ , ω may take on values as high as 50 rad/s, which suggests our frame rate of 50 frames per second may be only marginally sufficient. However, as stated above, the probability of finding these high ω is low so that measures such as the particle-scale rotational (spin) kinetic energy do not depend much on the frame rate.

Throughout the observed dynamics, energy is injected at the particle-scale; as the particles undergo collisions, this angular momentum is converted to translational momentum. Representative PDFs of the (x, y) velocity components v_x and v_y are plotted in Fig. 5a for bump size $l = 2$ mm. Note that at high ϕ , the PDFs of v_x and v_y are slightly different, likely due to a small tilt of the air table. Each curve is fit to a Gaussian distribution, shown as a solid line. While for high ϕ , the observed distributions fall off faster than a Gaussian, the agreement is good for low to intermediate values of ϕ . This agreement contrasts with the behavior reported for granular gases driven from the boundaries, where distributions fall off more slowly than Gaussian.^{21,29–35}

We can understand this difference by considering that the active spinners, unlike traditional granular gases, have a randomized, particle-scale origin to their translational velocities. This process appears to generate conditions more akin to the molecular chaos necessary to generate a Gaussian distribution. For an ideal gas in thermodynamic equilibrium, the probability of finding a particle at a speed $v \equiv \sqrt{v_x^2 + v_y^2}$ is given by the Maxwell-Boltzmann distribution, which in two dimensions is

$$P(v) = \frac{mv}{kT} \exp\left[-\frac{mv^2}{2kT}\right] \quad (2)$$

where m is the mass of the particle, k is the Boltzmann constant and T is the temperature. Our system differs from an ideal gas in several important ways: collisions are dissipative, the system is not in equilibrium (only steady-state), and the particles display collective motion.

Nonetheless, we find that the Maxwell-Boltzmann distribution is able to capture the main features of our observed distributions,

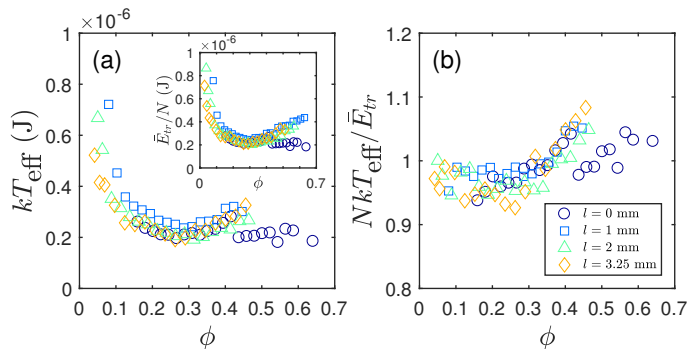


Fig. 6 (a) Thermal-like energy kT_{eff} obtained from fits to the Maxwell-Boltzmann distribution (Eq. 2), as a function of packing fraction ϕ . Inset shows the mean translational energy per particle \bar{E}_{tr}/N as a function of ϕ . Data points at very low ϕ (where $\bar{E}_{tr}/N > 1 \times 10^{-6}$ J and the Maxwell-Boltzmann fit is poor) are not shown. (b) Ratio of kT_{eff} and \bar{E}_{tr}/N , as a function of ϕ . Legend in (b) applies to all panels.

particularly at intermediate ϕ . As can be seen in Fig. 5b, the data at six representative values of ϕ (all with bump size $l = 2$ mm) can be fit by Eq. 2, shown with solid lines. At low ϕ , the quality of the fit may be influenced by insufficient collisions to generate a mixing of energy between degrees of freedom, and at high ϕ caging effects⁴² may similarly disrupt the exploration of phase space at high value of v . Note that we can also obtain an effective thermal energy kT_{eff} from the Gaussian fits of Fig. 5a; these values of kT_{eff} are very similar to those found by fitting Eq. 2, and thus predict $P(v)$ well (see dashed lines in Fig. 5b).

In order to deepen the analogy between the thermal-like kT_{eff} parameter (obtained from fits to Eq. 2), and the average kinetic energy, we examine how they vary with l and ϕ . Each dataset for which the data was well-captured by the Maxwell-Boltzmann distribution (e.g. the middle 4 of the 6 datasets in Fig. 5b), is examined in Fig. 6. In panel (a), we observe that the fit value of kT_{eff} is an approximately parabolic function of ϕ , and that this function is independent of bump size. The exception is at high ϕ for $l = 0$ mm, where there is a sudden jump to a lower, constant value above $\phi \approx 0.42$.

In a thermal system, the value of kT_{eff} would be determined by the average translational kinetic energy of the particles in the system, because both v_x and v_y add $\frac{1}{2}kT$. We measure the average total translational kinetic energy \bar{E}_{tr} in the system by summing $\frac{1}{2}mv^2$ over all N particles, and doing an ensemble average in time. The inset to panel (a) plots \bar{E}_{tr} on a per-particle basis, and it displays a similar trend to kT_{eff} . A direct comparison is shown in panel (b), where the ratio $NkT_{\text{eff}}/\bar{E}_{tr} = 1$ corresponds to thermal-like behavior. We find approximately agreement over a wide range of ϕ values. For $\phi \lesssim 0.3$, the ratio is slightly less than 1 because the Maxwell-Boltzmann fits underestimate the probability of high speeds. At higher ϕ , the fits overestimate the probability of high speeds (see $\phi = 0.464$ in Fig. 5b), which causes the ratio to go up.

3.3 Partition of energy

Continuing the analogy to thermal systems, we also consider the rotational degrees of freedom for each particle, measured from their spinning dynamics. As done for the translational kinetic

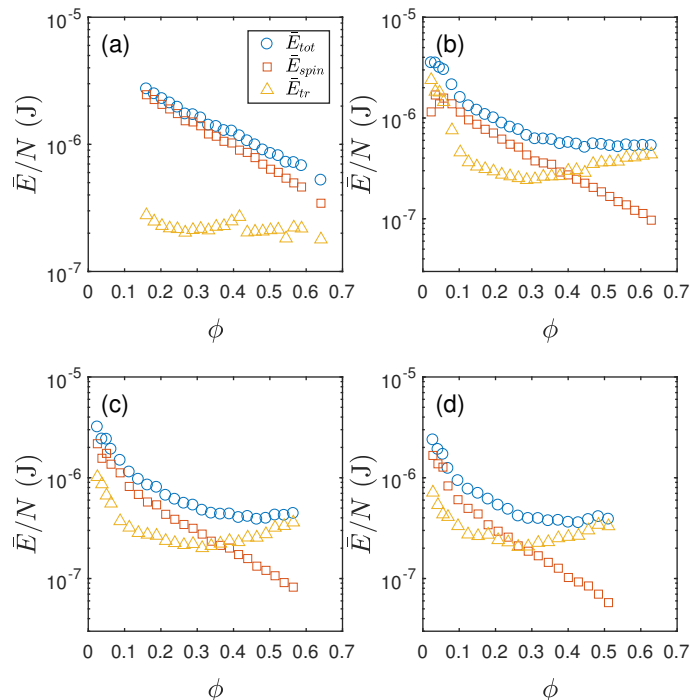


Fig. 7 Mean translational energy \bar{E}_{tr} , rotational energy \bar{E}_{spin} and total energy \bar{E}_{tot} per particle as a function of the packing fraction ϕ for (a) $l = 0$ mm, (b) $l = 1$ mm, (c) $l = 2$ mm, and (d) $l = 3.25$ mm. Legend in (a) applies to all panels. Note that the maximum packing fraction we can achieve depends on l , due to the additional space occupied by the bumps.

energy, we measure the average total rotational (spin) kinetic energy \bar{E}_{spin} by summing $\frac{1}{2}I\omega^2$ over all N particles, and doing an ensemble average in time. This gives a total kinetic energy $\bar{E}_{tot} = \bar{E}_{tr} + \bar{E}_{spin}$. Because the bumps hinder the spinning dynamics of the particles, but also provide a mechanism for momentum transfer, we expect that the partition of energy will depend on the bump size l .

In Fig. 7, we plot \bar{E}_{tr} , \bar{E}_{spin} and \bar{E}_{tot} , on a per-particle basis, as a function of ϕ , for all four bump sizes (the four panels). For all four values of l , \bar{E}_{spin}/N decreases approximately exponentially with ϕ . This decrease arises because the time between collisions decreases with ϕ , which prevents particles from accelerating to high ω ; the same effect was visible in Fig. 4.

For particles without bumps, Fig. 7a shows that \bar{E}_{tr}/N is roughly constant (with a small jump to lower energy at $\phi \approx 0.42$); this is the same data that was shown in Fig. 6. At all values of ϕ , \bar{E}_{tr}/N is considerably smaller than \bar{E}_{spin}/N , due to a lack of strong collisional transfer of momentum between the degrees of freedom. As a result, $\bar{E}_{tot} \approx \bar{E}_{spin}$ and also decreases roughly exponentially with ϕ , on a per-particle basis.

A very different behavior is observed for particles with bumps (Fig. 7b-d). In all three cases, \bar{E}_{tr}/N starts to exceed \bar{E}_{spin}/N at intermediate ϕ . For these systems, the total energy per particle becomes fairly constant for $\phi \gtrsim 0.3$. Interestingly, for larger bump sizes at high ϕ (Fig. 7c+d), a small increase in \bar{E}_{tot}/N can even be observed. This represents a strong collective effect: adding a particle to the system gives all individual particles more en-

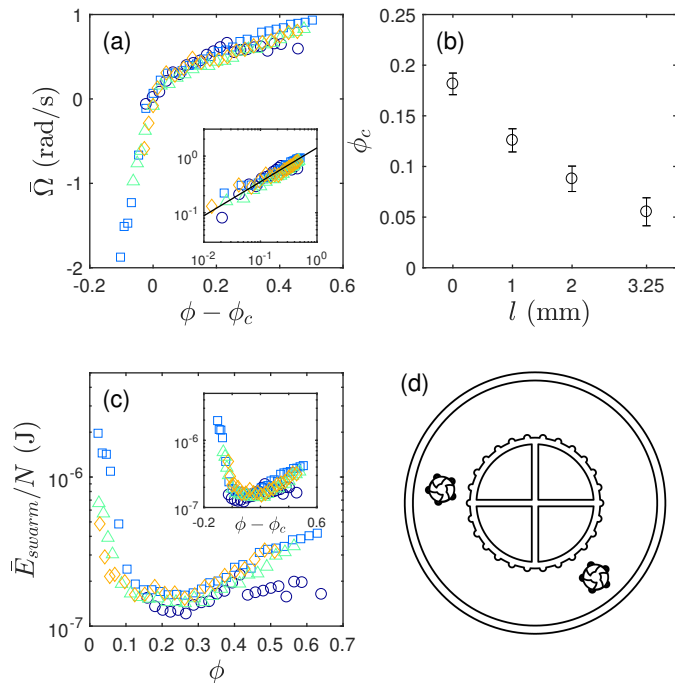


Fig. 8 (a) Mean orbital velocity of the ensemble $\bar{\Omega}$ as a function of reduced packing fraction $\phi - \phi_c$ for the four different particles used. Same symbols as in Fig. 6. Inset shows that for $\phi > \phi_c$, $\bar{\Omega} \propto (\phi - \phi_c)^{0.6}$ (solid line). (b) Packing fraction at which $\bar{\Omega} \approx 0$ for each bump size l . Error bars denote ± 1 particle. (c) Mean energy stored in swarming motion \bar{E}_{swarm} as a function of $\phi - \phi_c$. Same symbols as in Fig. 6. Inset shows the same data as a function of ϕ . (d) Drawing of the experiments with an inner boundary. The outside diameter of the inner boundary is 80 mm while the bumps have the same size and spacing as particles with $l = 2$ mm.

ergy, despite an increase in the frequency of dissipative collisions. Although \bar{E}_{rot} still decreases here, \bar{E}_{tr} rises more rapidly, which could be explained by the increased number of collisions allowing for a more effective coupling of rotational and translational degrees of freedom. Another phenomenon that may contribute to the rise of \bar{E}_{tot} is that the air flow resistance of the porous table surface may increase as ϕ is increased, leading to higher flow air flow rates *through* the particles and hence more torque. This effect is expected to be most noticeable for particles with large bumps, as a bigger fraction of their area "blocks" the pores of the air table.

3.4 Collective behavior and symmetry-reversal

To study the collective behavior arising through symmetry-reversal, we examine the average orbital rotation rate of the ensemble, $\bar{\Omega}$, calculated using Eq. 1. As shown in Fig. 8a, $\bar{\Omega}(\phi - \phi_c)$ is a universal function, independent of l . As such, the transition depicted schematically in Fig. 3 occurs identically for all four different particle types. At low ϕ , $\bar{\Omega}$ is negative (CW), but switches to positive values (CCW) as ϕ is increased. Although this effect is universal, the critical packing fraction ϕ_c at which the transition occurs depends on the bump size l ; values are given in Fig. 8b. The larger the frictional coupling, the lower the critical value of ϕ . This observation highlights the importance of the coupling between rotational and translational degrees of freedom

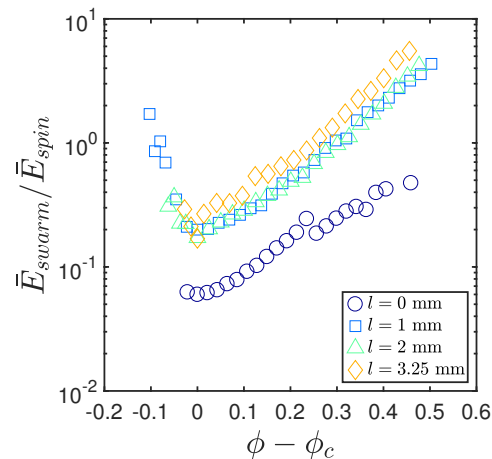


Fig. 9 Ratio of the energy stored in swarming motion \bar{E}_{swarm} to the mean particle-scale rotational energy \bar{E}_{spin} , as a function of $\phi - \phi_c$.

in the collective motion of these materials, which is governed by the interparticle interactions. Note that particles without bumps, although lacking geometric friction, still have ordinary frictional interactions. Hence, even for these systems, the rotational and translational degrees of freedom are coupled. It is noteworthy that Farhadi *et al.*³⁶ find a transition point in the velocity distributions of bump-less particles at a similar packing fraction ($\phi \approx 0.2$).

The swarm-like collective motion shown in Fig. 3 can additionally be characterized by the mean kinetic energy associated with that motion. We compute a quantity \bar{E}_{swarm} by summing $\frac{1}{2}mv_{\parallel}^2$ over all N particles, and doing an ensemble average in time. Recall that v_{\parallel} is the orbital (azimuthal) velocity of each particle, relative to the center of the arena. Since $E_{swarm} \propto v_{\parallel}^2$, \bar{E}_{swarm} is positive for both CW and CCW motion and a minimum is expected where v_{\parallel} has low absolute values. Although at ϕ_c there is no net orbital motion ($\sum v_{\parallel} \approx 0$), individual particles may still have a small, finite absolute v_{\parallel} . Therefore, the minimum of \bar{E}_{swarm} does not necessarily coincide with ϕ_c , which is indeed not the case (Fig. 8c and inset). Rather, much like kT_{eff} and \bar{E}_{tr} , \bar{E}_{swarm} is roughly universal function of ϕ . This can be understood by recalling that $E_{swarm} = \frac{1}{2}mv_{\parallel}^2$ is a component of $E_{tr} = \frac{1}{2}mv^2$, since v_{\parallel} is a component of v . Thus, like kT_{eff} and \bar{E}_{tr} , at large ϕ , \bar{E}_{swarm} is lower for the particles without bumps ($l = 0$ mm), again reflecting these particles' inefficiency at transferring momentum between degrees of freedom.

In a system where individual particles do not spin, but the collection of particles orbits around a common axis, \bar{E}_{spin} would be zero and \bar{E}_{swarm} maximized. Therefore, the ratio of \bar{E}_{swarm} to \bar{E}_{spin} is an order parameter describing the collective behavior in the system. As shown in Fig. 9, for all particle types, \bar{E}_{spin} dominates at low to intermediate ϕ , and this ratio is therefore less than 1. For particles with bumps, the ratio $\bar{E}_{swarm}/\bar{E}_{spin}$ rapidly increases to well above unity as ϕ is increased: this indicates that collective motion dominates over individual particle spin. For the largest bumps, the collective effect above ϕ_c is observed to be largest. For particles without bumps, $\bar{E}_{swarm}/\bar{E}_{spin} < 1$ for all ϕ . Thus, in the absence of sufficient geometric friction, the individual contributes little to the collective.

3.5 Understanding the transition

We have identified that frictional interactions between particles govern the transition from CW-individual to CCW-collective motions that was illustrated in Fig. 3. Because there are boundaries to the arena, two parameters are changing as ϕ is increased: the frequency of particle-particle collisions (increasing), and the relative importance of particle-boundary collisions (decreasing). At low values of ϕ , most collisions are with the outer wall, and as the particles spin CCW around their own axis, this tends to give the particles momentum in the CW direction (negative $\bar{\Omega}$).

Therefore, we test the hypothesis that the transition occurs because particles close to the center of the arena act like an inner boundary for the particles further out. We conduct tests using an artificial inner boundary of diameter 80 mm, either with or without bumps mimicking a group of $l = 2$ mm particles. Two particles with $l = 2$ mm are placed within this annular arena, as shown in Fig. 8d. For three different cases – no inner boundary, smooth inner boundary, rough inner boundary – we compute the mean orbital velocity $\bar{v}_{||}$.

For the case without an inner boundary (circular arena), the particles have only the outer boundary to collide with and we observe CW motion with $\bar{v}_{||} \approx 6$ cm/s. For the case with a smooth inner boundary, nearly symmetric collisions occur with either the inner or outer boundaries; this results in $\bar{v}_{||} \approx 0$. For the case with a rough inner boundary, the transfer of rotational energy to translational energy is more effective at the inner boundary than at the outer boundary due to the geometric friction provided by the bumps; this results in CCW motion $\bar{v}_{||} \approx 2$ cm/s, breaking the symmetry in the opposite direction compared to the circular arena.

These same principles are at work in the main observation of symmetry-reversal from CW to CCW motion in a circular arena. As ϕ increases, the particles nearer the center start to act as an object which provides a source of momentum transfer for the particles further out. This changes the direction of the collective motion from a mis-match with the particle-scale spin to one that matches (CCW). The effectiveness of this mechanism depends on the bump size l , explaining the decreasing $\phi_c(l)$ trend shown in Fig. 8b.

4 Conclusion

We experimentally study a granular gas composed of actively spinning disks, made rough using bumps. We observe interesting collective behavior, characterized by a transition of clockwise to counter-clockwise orbit of the particles with respect to center of the arena, at a critical volume fraction ϕ_c . By driving the particles through their rotational degree of freedom, we obtain a material that is in many ways like an ideal gas, with Gaussian PDFs for the velocity components v_x and v_y and a Maxwell-Boltzmann distribution of speeds. However, in contrast to gases, energy is not equally partitioned across the translational and rotational degrees of freedom, and we show that the partitioning depends on the geometric friction that the particles experience through their bumps. We demonstrate that the swarming of our materials is governed by this geometric friction, as ϕ_c depends strongly on the bump size, as does the ratio of energy stored in swarming motion

and individual spinning. Finally, we show that the direction of the swarming motion can be tuned by adjusting the boundaries of the material. Our findings demonstrate that the type of driving plays a crucial role in the statistical mechanics of granular gases, and highlights geometric friction as an important control parameter for the design of active materials with tunable mechanical properties.

Conflicts of interest

There are no conflicts to declare.

Acknowledgements

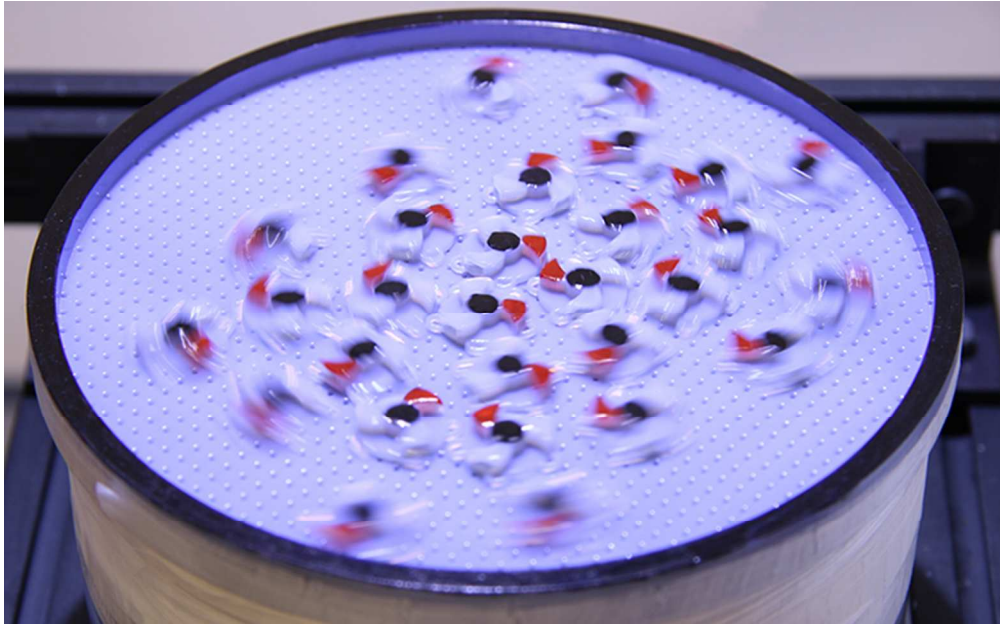
We thank Frédéric Lechenault and Daphne Klotsa for helpful conversations. We thank Michael Murphy for his help with particle design and exploratory experiments. We are grateful for funding from the National Science Foundation under grants DMR-1608097 (K.E.D) and the Research Triangle MRSEC DMR-1121107 (K.E.D. and G.R.).

References

- 1 R. Eelkema, M. M. Pollard, J. Vicario, N. Katsonis, B. S. Ramon, C. W. Bastiaansen, D. J. Broer and B. L. Feringa, *Nature*, 2006, **440**, 163–163.
- 2 T. Sanchez, D. T. Chen, S. J. DeCamp, M. Heymann and Z. Dogic, *Nature*, 2012, **491**, 431–434.
- 3 W. Bialek, A. Cavagna, I. Giardina, T. Mora, E. Silvestri, M. Viale and A. M. Walczak, *Proceedings of the National Academy of Sciences*, 2012, **109**, 4786–4791.
- 4 L. Berthier and J. Kurchan, *Nature Physics*, 2013, **9**, 310–314.
- 5 S. C. Takatori, W. Yan and J. F. Brady, *Physical Review Letters*, 2014, **113**, 028103.
- 6 S. Ramaswamy, *Annual Review of Condensed Matter Physics*, 2010, **1**, 323–345.
- 7 M. C. Marchetti, J.-F. Joanny, S. Ramaswamy, T. B. Liverpool, J. Prost, M. Rao and R. A. Simha, *Reviews of Modern Physics*, 2013, **85**, 1143.
- 8 A. M. Menzel, *Physics Reports*, 2015, **554**, 1–45.
- 9 S. Fürthauer, M. Neef, S. W. Grill, K. Kruse and F. Jülicher, *New Journal of Physics*, 2012, **14**, 023001.
- 10 G. S. Redner, M. F. Hagan and A. Baskaran, *Physical Review Letters*, 2013, **110**, 055701.
- 11 L. Soler and S. Sánchez, *Nanoscale*, 2014, **6**, 7175–7182.
- 12 J. Aragonés, J. Steimel and A. Alexander-Katz, *Nature Communications*, 2016, **7**, 11325.
- 13 N. H. Nguyen, D. Klotsa, M. Engel and S. C. Glotzer, *Physical Review Letters*, 2014, **112**, 075701.
- 14 S. Sabrina, M. Spellings, S. C. Glotzer and K. J. Bishop, *Soft matter*, 2015, **11**, 8409–8416.
- 15 B. C. van Zuiden, J. Paulose, W. T. Irvine, D. Bartolo and V. Vitelli, *Proceedings of the National Academy of Sciences*, 2016, 201609572.
- 16 G. Kokot, S. Das, R. G. Winkler, G. Gompper, I. S. Aranson and A. Snezhko, *Proceedings of the National Academy of Sciences*, 2017, **114**, 12870–12875.

- 17 J. Zhang and S. Granick, *Faraday discussions*, 2016, **191**, 35–46.
- 18 J.-C. Tsai, F. Ye, J. Rodriguez, J. P. Gollub and T. Lubensky, *Physical Review Letters*, 2005, **94**, 214301.
- 19 E. Altshuler, J. M. Pastor, A. Garcimartín, I. Zuriguel and D. Maza, *PloS one*, 2013, **8**, e67838.
- 20 C. Scholz and T. Pöschel, *Revista Cubana de Física*, 2016, **33**, 37–38.
- 21 C. Scholz and T. Pöschel, *Physical Review Letters*, 2017, **118**, 198003.
- 22 C. Scholz, M. Engel and T. Pöschel, *Nature Communications*, 2018, **9**, 931.
- 23 C. S. Campbell, *Annual Review of Fluid Mechanics*, 1990, **22**, 57–90.
- 24 H. M. Jaeger, S. R. Nagel and R. P. Behringer, *Reviews of modern physics*, 1996, **68**, 1259.
- 25 I. Goldhirsch and G. Zanetti, *Physical Review Letters*, 1993, **70**, 1619.
- 26 J. Eggers, *Physical Review Letters*, 1999, **83**, 5322.
- 27 V. Narayan, S. Ramaswamy and N. Menon, *Science*, 2007, **317**, 105–108.
- 28 G. D’Anna, P. Mayor, A. Barrat, V. Loreto and F. Nori, *Nature*, 2003, **424**, 909–912.
- 29 K. Nichol and K. E. Daniels, *Physical Review Letters*, 2012, **108**, 018001.
- 30 W. Losert, D. Cooper, J. Delour, A. Kudrolli and J. Gollub, *Chaos*, 1999, **9**, 682–690.
- 31 F. Rouyer and N. Menon, *Physical Review Letters*, 2000, **85**, 3676.
- 32 I. Aranson and J. Olafsen, *Physical Review E*, 2002, **66**, 061302.
- 33 A. Prevost, D. A. Egolf and J. S. Urbach, *Physical Review Letters*, 2002, **89**, 084301.
- 34 T. Van Noije and M. Ernst, *Granular Matter*, 1998, **1**, 57–64.
- 35 P. M. Reis, R. A. Ingale and M. D. Shattuck, *Physical Review E*, 2007, **75**, 051311.
- 36 S. Farhadi, S. Machaca, J. Aird, B. O. Torres Maldonado, S. Davis, P. E. Arriata and D. J. Durian, *Joint submission to Soft Matter*, 2018.
- 37 S. Papanikolaou, C. S. O’Hern and M. D. Shattuck, *Physical Review Letters*, 2013, **110**, 198002.
- 38 M. Workamp, *PhD thesis*, 2018.
- 39 D. Blair and E. Dufresne, *Particle-tracking code available at <http://physics.georgetown.edu/matlab>*, 2013.
- 40 M. R. D’Orsogna, Y.-L. Chuang, A. L. Bertozzi and L. S. Chayes, *Physical Review Letters*, 2006, **96**, 104302.
- 41 Y.-l. Chuang, M. R. D’Orsogna, D. Marthaler, A. L. Bertozzi and L. S. Chayes, *Physica D: Nonlinear Phenomena*, 2007, **232**, 33–47.
- 42 E. R. Weeks and D. A. Weitz, *Physical Review Letters*, 2002, **89**, 95704.

A swarm of active-spinner particles display a reversal of their swarming direction as their packing density is increased, an effect that can be enhanced by adding geometric friction between the particles.



64x39mm (300 x 300 DPI)